

**Braiding-based quantum control of a Majorana qubit built from quantum dots**Péter Boross<sup>1,2</sup> and András Pályi<sup>1,3</sup><sup>1</sup>*Department of Theoretical Physics, Institute of Physics, Budapest University of Technology and Economics, Műegyetem rkp. 3., H-1111 Budapest, Hungary*<sup>2</sup>*Institute for Solid State Physics and Optics, Wigner Research Centre for Physics, P.O. Box 49, H-1525 Budapest, Hungary*<sup>3</sup>*MTA-BME Quantum Dynamics and Correlations Research Group, Műegyetem rkp. 3., H-1111 Budapest, Hungary*

(Received 16 May 2023; revised 30 January 2024; accepted 7 February 2024; published 11 March 2024)

Topology-related ideas might lead to noise-resilient quantum computing. For example, it is expected that the slow spatial exchange (“braiding”) of Majorana zero modes in superconductors yields quantum gates that are robust against disorder. Here, we report our numerical experiments, which describe the dynamics of a Majorana qubit built from quantum dots controlled by time-dependent gate voltages. Our protocol incorporates nonprotected control, braiding-based protected control, and readout of the Majorana qubit. We use the Kitaev chain model for the simulations, and we focus on the case when the main source of errors is quasistatic charge noise affecting the hybridization energy splitting of the Majorana modes. We provide quantitative guidelines to suppress both diabatic errors and disorder-induced qubit dephasing, such that a fidelity plateau is observed as the hallmark of the topological quantum gate. Our simulations predict realistic features that are expected to be seen in future braiding experiments with Majorana zero modes and other topological qubit architectures.

DOI: [10.1103/PhysRevB.109.125410](https://doi.org/10.1103/PhysRevB.109.125410)**I. INTRODUCTION**

Majorana zero modes (MZMs) as bound states in topological superconductors might be used as building blocks of future quantum technology, enabling topologically protected quantum-logical qubit operations [1–3]. This opportunity has triggered intense research efforts in the past decade [4–13]. The protection of the quantum information encoded in such a Majorana qubit is, however, incomplete [14–27]. To assess the technological potential of Majorana qubits, it is critical to understand their decoherence mechanisms.

Due to their topological protection, Majorana qubits might serve as long-lived quantum memory elements, hence the decoherence properties of idle qubits are of interest [15–19,24,28–35]. Majorana qubits could also serve as building blocks of quantum processors, where they are subject to electromagnetic control fields, e.g., controlling the spatial exchange of the MZMs [3,36]. Such a MZM exchange can yield a single-qubit  $\pi/2$  gate, and can also be useful to perform two-qubit gates, e.g., a CNOT [36–38]. (Note that other works propose “braiding without braiding,” i.e., measurement-based quantum gates that avoid spatial exchange MZMs [20,39,40].)

Reference [3] proposed to braid MZMs in one-dimensional (1D) topological superconductors to achieve topologically protected quantum gates. Advantages and limitations of this topological protection of braiding-based gates has been the subject of many theoretical works since then. Models of MZM braiding range from the effective description restricted to the degenerate subspace [22,25,26,41–44], through the Kitaev chain model [23,45–47], to the Rashba wire model [36,48].

MZMs are also predicted in engineered topological superconductors, where an effective Kitaev chain is formed by a register of quantum dots proximitized by nearby superconductors [49–53]. Recent experimental progress with quantum-dot chains, featuring charge shuttling in a nine-dot array [54], spin qubit operation in six-dot arrays [55,56], the triple Andreev dot chain [57], and the realization of the minimal Kitaev chain [58] strengthen the feasibility of the quantum-dot approach to MZMs. In such quantum dots, often used as spin qubit registers, a key qubit decoherence mechanism is the fluctuation of the on-site energies of the dots, attributed to electromagnetic fluctuations of the environment, including  $1/f$  charge noise [35,59–65].

In this work, we propose a few-dot setup and a control scheme, which could be used to experimentally demonstrate braiding-based gates with MZMs based on quantum dot arrays [50,51,66]. We perform numerical experiments to predict the quality of braiding-based gates in the presence of charge noise, which we incorporate in our model as quasistatic disorder. Our numerical results show diabatic errors for short braiding times as well as qubit dephasing effects for long braiding times. We identify an experimentally relevant parameter range where a future experiment can find “fidelity plateaus” as fingerprints of topologically protected quantum gates.

The rest of the paper is organized as follows. In Sec. II, we introduce the setup of our numerical experiment and highlight the main steps of our braiding-based protocol. In Sec. III, we describe the nonadiabatic dynamics of the system in the absence of any disturbances. In Sec. IV, we show the effect of the quasistatic disorder on our protocol. We discuss

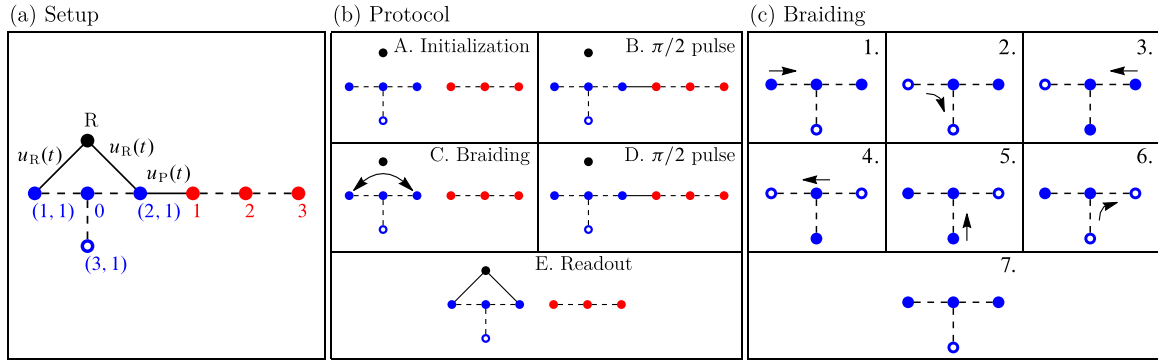


FIG. 1. Protocol to demonstrate a braiding-based  $\pi/2$  gate on a Majorana qubit. (a) Blue:  $Y$  junction built from Kitaev chains. Red: a straight Kitaev wire. Blue and red together form a Majorana qubit. Black: readout dot. (b) The five-step protocol, analogous to a Ramsey protocol, aiming to detect the braiding-based  $\pi/2$  gate: A, Initialization; B, First  $\pi/2$  pulse; C, Braiding; D, Second  $\pi/2$  pulse; E, Readout. (c) Procedure of a single MZM exchange used in step C, Braiding.

implications and follow-up ideas in Sec. V, and we conclude in Sec. VI.

## II. PROTOCOL TO DEMONSTRATE A BRAIDING-BASED $\pi/2$ GATE OF A MAJORANA QUBIT

Here we introduce a model and a protocol, suitable for the experimental demonstration of the braiding-based  $\pi/2$  quantum gate of a Majorana qubit. The setup is sketched in Fig. 1(a). It consists of three units: a  $Y$  junction built from Kitaev chains (blue), a straight Kitaev wire (red), and a readout dot (black). Dashed lines denote connections via electron tunneling and Cooper-pair creation and annihilation. Solid lines denote connections via tunneling only. Filled and empty circles depict different on-site energies. This setup consists of two Kitaev chains (blue filled circles and red filled circles), and hence it can host a Majorana qubit in its ground-state subspace. Based on Refs. [50–52,58,66], we envision that proximitized quantum dot arrays can realize such a few-site Kitaev model.

The  $Y$  junction consists of three regular Kitaev chains (legs) and a central site. Each Kitaev chain can be described by the following Hamiltonian [2]:

$$H_c^{(n,N_c)} = \sum_{i=1}^{N_c-1} (v c_{n,i}^\dagger c_{n,i+1} + \Delta_n c_{n,i}^\dagger c_{n,i+1}^\dagger + \text{H.c.}) + \sum_{i=1}^{N_c} \mu_{n,i}(t) c_{n,i}^\dagger c_{n,i}, \quad (1)$$

where  $N_c$  is the length of the legs (it is set to  $N_c = 1$  in Fig. 1),  $c_{n,i}^\dagger$  and  $c_{n,i}$  are the creation and annihilation operators on the  $i$ th site of the  $n$ th chain ( $n \in \{1, 2, 3\}$ ),  $v$  denotes the nearest-neighbor hopping amplitude,  $\Delta_n$  is the  $p$ -wave superconducting pairing amplitude in the  $n$ th chain, and  $\mu_{n,i}(t)$  is the site- and time-dependent on-site energy of the  $i$ th site of the  $n$ th chain.

Based on the Hamiltonians of the legs in Eq. (1), the Hamiltonian of the  $Y$  junction is written as

$$H_Y = \sum_{n=1}^3 H_c^{(n,N_c)} + \mu_0 c_0^\dagger c_0 + \sum_{n=1}^3 (v c_0^\dagger c_{n,1} + \Delta_n c_0^\dagger c_{n,1}^\dagger + \text{H.c.}), \quad (2)$$

where index 0 denotes the central site, and the superconducting pair potential is  $\Delta_1 = \Delta e^{i\varphi}$ ,  $\Delta_2 = \Delta e^{-i\varphi}$ , and  $\Delta_3 = -\Delta$ , with  $\Delta > 0$ . For concreteness, we set  $\varphi = \pi/2$  in our simulations.

Another building block of the Majorana qubit is a straight Kitaev wire, depicted as filled red circles in Fig. 1. Its length is chosen, for simplicity, to have the same length as the topological region of the  $Y$  junction, which is 3 in the case of  $N_c = 1$ . Thus the corresponding Hamiltonian is

$$H_W = \sum_{i=1}^{2N_c} (v c_i^\dagger c_{i+1} + \Delta_W c_i^\dagger c_{i+1}^\dagger + \text{H.c.}) + \sum_{i=1}^{2N_c+1} \mu_i c_i^\dagger c_i, \quad (3)$$

where  $\Delta_W = \Delta e^{-i\varphi}$ .

With the purpose of reading out the parity of the  $Y$  junction, an additional site, the *readout dot* [19,20,67,68] denoted by “R” in Fig. 1(a), is coupled to the system. The Hamiltonian of the full system reads

$$H = H_Y + H_W + \mu_R c_R^\dagger c_R + (u_P(t) c_{2,N_c}^\dagger c_1 + \text{H.c.}) + \sum_{n=1}^2 (u_R(t) c_R^\dagger c_{n,N} + \text{H.c.}). \quad (4)$$

Here,  $u_P(t)$  is the hopping amplitude between the rightmost site of the  $Y$  junction and the leftmost site of the straight Kitaev wire, which is required in the (nonprotected)  $\pi/2$  pulses of the experimental protocol; see below. Furthermore,  $u_R(t)$  is the tunneling amplitude between the readout dot and the two ends of the  $Y$  junction, which is utilized for parity-to-charge conversion in the readout step of the experimental protocol.

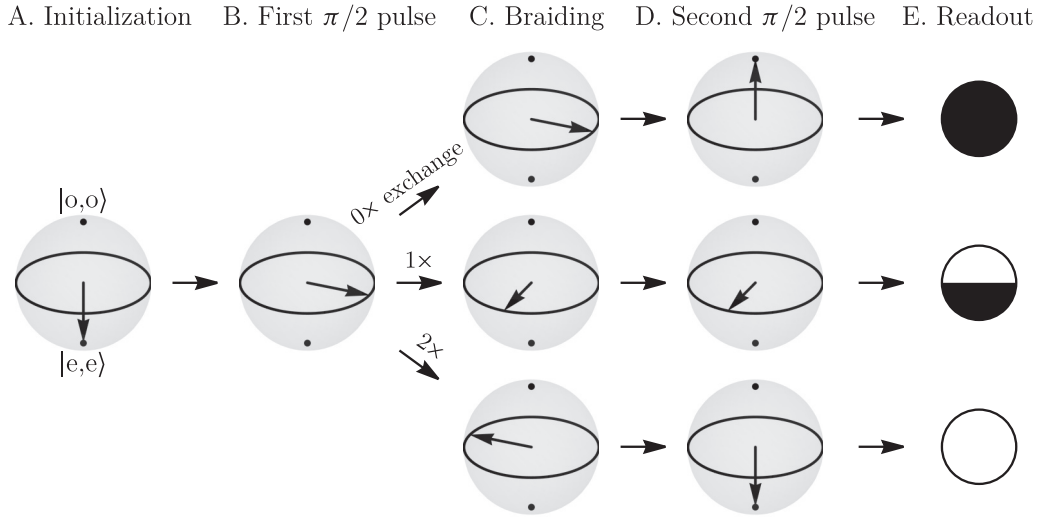


FIG. 2. Ramsey-type experiment to detect the braiding-based  $\pi/2$  gate on the Majorana qubit. Error-free evolution of the qubit Bloch vector, shown after each step (A)–(D) of the protocol, cf. Table I. Qubit basis states are  $|e,e\rangle$  and  $|o,o\rangle$ . The last column shows the expected value of the readout dot occupation at the end of the protocol. The three paths correspond to the protocol with 0, 1, and 2 exchanges.

The  $Y$  junction and the straight Kitaev wire can host two MZMs each, and their composite system can host a Majorana qubit. By default, both the  $Y$  junction and the straight Kitaev wire are tuned to their topological fully dimerized limit, and hence the ground state of their composite system is fourfold-degenerate. The four ground states will be denoted as  $|e, e\rangle$ ,  $|e, o\rangle$ ,  $|o, e\rangle$ ,  $|o, o\rangle$ , with  $e$  ( $o$ ) being a reference to the even (odd) fermion-number parity of each unit. The topological fully dimerized limit is defined by setting (i) the hopping amplitudes and the absolute value of the superconducting pair potentials equal to each other, i.e.,  $\Delta = v$ , and (ii) the on-site potentials to zero. This limit implies MZMs that are perfectly localized at the end sites of the topological regions. The protocol we propose to demonstrate braiding is similar to the well-known Ramsey experiment, as shown in Fig. 2 and Table I. The key difference is that most often the Ramsey experiment aims to characterize unwanted dephasing dynamics (see, e.g., Fig. 10 of Ref. [19]), whereas here we use this scheme to characterize an intentional, braiding-based  $\pi/2$  gate.

Our Ramsey-type protocol consists of five steps: (A) initialization, (B) first  $\pi/2$  pulse, (C) braiding, (D) second  $\pi/2$  pulse, and (E) readout, detailed in the subsections below. The development of the many-body wave function at the key points of the protocol is shown in Table I, and the development

of the corresponding Majorana qubit polarization vector is shown in Fig. 2. As seen in Table I and Fig. 2, we consider three different cases: when no braiding is done ( $0\times$  exchange), when a single exchange is performed ( $1\times$  exchange), and when two exchanges are performed ( $2\times$  exchange). In the table, we use the notation  $|p_Y, p_W, n_R\rangle$ , where  $p_Y \in \{e, o\}$  ( $p_W \in \{e, o\}$ ) is the parity of the  $Y$  junction (straight wire), and  $n_R \in \{0, 1\}$  is the occupation of the readout dot. Table I shows the wave functions in an idealized, error-free case, when there is no disorder, no timing error, no leakage from the computational subspace, etc. Figure 2 shows the polarization vector of the Majorana qubit after each of the first four steps of the protocol, with the last column showing the readout dot occupation expectation value, which can be measured upon readout.

The last step of the protocol is the measurement of the charge of the readout dot. The measurement probabilities can be read off the last row (“Readout”) of Table I as follows. For  $0\times$  exchange, the measurement probability of finding a charge in R is 1, for  $1\times$  exchange it is 0.5, and for  $2\times$  exchange it is 0. This probability (which is the same as the charge expectation value of the readout dot) carries the parity information of the  $Y$  junction: if it is zero, that signals that the  $Y$  junction was in the even state after the second  $\pi/2$  pulse, and before starting the parity-to-charge conversion

TABLE I. Error-free evolution of the many-body wave function during the Ramsey-type protocol. Three columns correspond to the protocol with 0, 1, and 2 exchanges. The wave function shown in each row is the state at the end of that step.

	$0\times$ exchange	$1\times$ exchange	$2\times$ exchanges
A. Initialization	$ e, e, 0\rangle$		
B. First $\pi/2$ pulse	$\frac{1}{\sqrt{2}}  e, e, 0\rangle + \frac{1}{\sqrt{2}}  o, o, 0\rangle$		
C. Braiding	$\frac{1}{\sqrt{2}}  e, e, 0\rangle + \frac{1}{\sqrt{2}}  o, o, 0\rangle$	$\frac{1}{\sqrt{2}}  e, e, 0\rangle + \frac{i}{\sqrt{2}}  o, o, 0\rangle$	$\frac{1}{\sqrt{2}}  e, e, 0\rangle - \frac{1}{\sqrt{2}}  o, o, 0\rangle$
D. Second $\pi/2$ pulse	$ o, o, 0\rangle$	$\frac{1-i}{2}  e, e, 0\rangle + \frac{1+i}{2}  o, o, 0\rangle$	$ e, e, 0\rangle$
E. Readout	$i  e, o, 1\rangle$	$\frac{1-i}{2}  e, e, 0\rangle - \frac{1-i}{2}  e, o, 1\rangle$	$ e, e, 0\rangle$

(e.g.,  $2 \times$  exchange); if it is one, that signals the odd parity (e.g.,  $0 \times$  exchange).

In what follows, we describe the five steps of the protocol in detail.

### A. Initialization

At the beginning of the protocol, the coupling between the  $Y$  junction and the straight wire, and the coupling between the  $Y$  junction and the readout dot, are turned off, i.e.,  $u_P = 0$  and  $u_R = 0$ . All the on-site potentials are set to zero, except in the third leg of the  $Y$  junction, where they are set to the value  $\xi = 4v$ , adjusted well over the critical value  $2v$ . We assume that the Majorana qubit is initialized in the state  $|e, e\rangle$ . This implies that the physically available part of the four-dimensional ground-state subspace is the two-dimensional subspace spanned by the globally even ground states  $|e, e\rangle$  and  $|o, o\rangle$ . The two states form the computational basis for the Majorana qubit. We also assume that the dot is initialized to be empty.

### B. First $\pi/2$ pulse

The second step is a nonprotected  $\pi/2$  rotation of the Majorana qubit, i.e., a rotation in the subspace spanned by  $|e, e\rangle$  and  $|o, o\rangle$ . We will refer to this as a rotation around the  $y$  axis of the Bloch sphere. (Note that this is an implicit condition for the relative global phase of the two-qubit basis states, which we have not defined explicitly.) Here, a balanced superposition of the basis states is achieved by switching on the tunnel coupling  $u_P$ . We apply a sine-squared shaped pulse which has the form

$$u_P(t) = u_{P,\max} \sin^2(\pi t/T_P) \quad \text{if } 0 \leq t \leq T_P, \quad (5)$$

where the duration  $T_P = h/(4u_{P,\max})$  of the pulse is set to provide a  $\pi/2$  gate. To avoid quasiparticle excitation, we use a weak pulse,  $u_{P,\max} = 0.25v$ . Note that this gate is not topologically protected [24,69,70]; i.e., errors in the tunnel pulse strength or duration lead to gate errors that are not suppressed by increasing the system size or slower operation.

### C. Braiding

The next step is the braiding of the MZMs localized on sites (1,1) and (2,1), making use of the site (3,1) of the  $Y$  junction. MZMs can be exchanged by means of the steps shown in Fig. 1(c). Moving MZMs is realized by ramping up (down) the on-site energies to the value  $\xi = 4v$  (zero). These we do by using sine-squared pulses. The shape of the pulse for the ramp-up reads

$$\mu_{n,i}(t) = \xi \sin^2\left(\frac{\pi t}{2T_{\text{ramp}}}\right) \quad \text{if } 0 \leq t \leq T_{\text{ramp}}, \quad (6)$$

where  $T_{\text{ramp}}$  is the ramping time, i.e., the duration through which an on-site potential is varied. For longer chains, i.e.,  $N_c > 1$ , ramp-up and ramp-down of on-site potentials in each leg is performed consecutively, site-by-site. Adiabatic exchange of the modes will create a  $\pi/2$  phase difference [3] between the basis state  $|e, e\rangle$  and  $|o, o\rangle$ . This phase difference is expected to be robust against imperfections of the path of control parameters, including quasistatic disorder, in the limit

of adiabatic control and large system size; characterizing this robustness in the presence of diabatic errors and small system sizes is one of the goals of the numerical experiments in the next sections.

As we argue below, performing this protocol with two MZM exchange, providing a  $\pi$  gate, should be used as an important control experiment. We will denote the number of exchanges by  $N_E$ . Furthermore, as seen from Fig. 1(c), the full duration of the Braiding step is  $T_B = 6N_c N_E T_{\text{ramp}}$ . Note also that we use the term ‘‘exchange’’ to denote a single (clockwise or counterclockwise) exchange of two MZMs, whereas we use the term ‘‘braiding’’ to describe any combination of MZM exchanges.

### D. Second $\pi/2$ pulse

After the braiding step, a second nonprotected  $\pi/2$  pulse is applied, to do a rotation around the  $y$  axis. Naturally, the many-body state after this step (row 4 of Table I) depends on the number of exchanges done during Braiding.

### E. Readout

In our protocol, readout of the parity of the  $Y$  junction is based on parity-to-charge conversion [19,20,67,68]. We follow the scheme described in [67]: conversion is performed by switching on the two tunnel couplings  $u_R$  for an appropriate duration, and reading out the charge of the readout dot afterwards. The tunnel pulse converts the fermion-number parity of the  $Y$  junction to the charge of the dot. The charge readout is assumed to be perfect, and to yield 0 or 1.

For parity-to-charge conversion, we use sine-squared tunnel pulses:

$$u_R(t) = u_{R,\max} \sin^2(\pi t/T_R) \quad \text{if } 0 \leq t \leq T_R, \quad (7)$$

where  $u_{R,\max}$  is the strength of the parity-to-charge conversion, and  $T_R = h/(4u_{R,\max})$  is the duration for ideal conversion. In our simulations, we use  $u_{R,\max} = 0.25v$ . Note that this parity-to-charge conversion scheme is not ‘‘protected,’’ in the sense that small perturbations, e.g., on-site energy fluctuations, or errors in the tunnel pulse strength or duration, lead to readout errors without any exponential suppression [67]. (For alternative parity-to-charge conversion schemes, and their error mechanisms, see, e.g., Refs. [19,20,39,40,71–73].)

## III. DIABATIC ERRORS OF A PERFECT MAJORANA QUBIT

Before describing the effect of quasistatic disorder, we characterize the braiding-based  $\pi/2$  gate in a clean, perfectly controlled system. We performed numerical simulations of the protocol described above using the time-dependent Bogoliubov–de Gennes (BdG) formalism. Details are described in Appendix. The BdG formalism allows for efficient simulations: for example, the many-body Fock space of the eight-site setup in Fig. 1(a) has dimension  $2^8 = 256$ , growing exponentially with increasing system size  $N_c$ , whereas the space of BdG wave functions has dimension  $2 \times 8 = 16$ , growing linearly with increasing system size  $N_c$ .

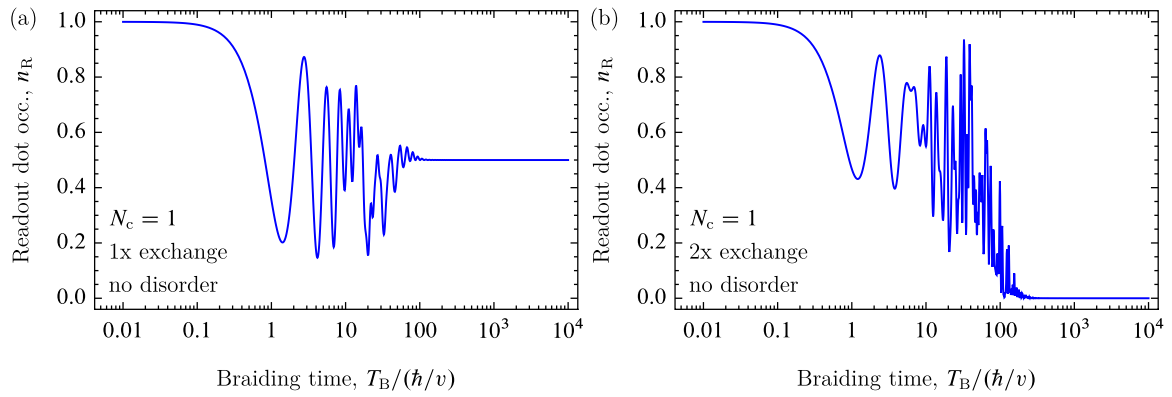


FIG. 3. In a disorder-free system, a braiding-based  $\pi/2$  gate implies a fidelity plateau for long braiding times. Readout dot occupation is shown as a function of the braiding time, for the setup with eight quantum dots ( $N_c = 1$ ), obtained from our numerical simulation of a disorder-free system. (a) Protocol with one exchange of the Majorana zero modes in the  $Y$  junction. (b) Protocol with two exchanges. For short braiding times, braiding does not affect the dynamics resulting in  $n_R \approx 1$ . For intermediate braiding times, diabatic errors dominate the data. In the adiabatic limit ( $T_B \rightarrow \infty$ ), readout dot occupation shows a fidelity plateau at (a)  $1/2$  and (b)  $0$ , as predicted in Table I.

We solve the time-dependent BdG-Schrödinger equation numerically by discretizing the time axis, approximating the time dependence of the parameters by steplike dependence, and evaluating the propagator for each time step by exponentiating the instantaneous BdG Hamiltonian matrix. Recall that all of our control pulses have sine-squared shape. We call each half-period of each sine-squared pulse an *elementary step* in our protocol. For each elementary step, having duration  $T$ , we choose the time discretization step as  $\Delta t = \min\{\hbar/v, T/150\}$ .

In our numerical experiment, we aim to characterize the braiding-based  $\pi/2$  gate via the statistics of the measurement of the readout dot charge. This is a realistic constraint: in a real experiment, the experimenter can indeed perform a charge measurement, but has no access to the many-body wave function (let alone any of the BdG wave functions). Hence, the target quantity of our simulations is the readout dot occupation,  $n_R = \langle \Psi_f | c_R^\dagger c_R | \Psi_f \rangle$ , where  $\Psi_f$  is the final state, i.e., the many-body state of the system after the parity-to-charge conversion.

The numerical result for this readout dot occupation, for a protocol with a braiding containing  $1 \times$  exchange, is shown in Fig. 3(a) as a function of braiding time  $T_B$ . This result corresponds to the smallest system size  $N_c = 1$ , i.e., to the eight-site setup shown in Fig. 1(a). For short braiding times,  $T_B \lesssim 0.1\hbar/v$ , the exchange protocol is so fast that the wave function is almost unchanged during the braiding because the system has no time to respond to the time dependence of the Hamiltonian. Thus in this limit, the final wave function is close to the one corresponding to no exchange (see “ $0 \times$  exchange” column in Table I). In the adiabatic limit, however, i.e., for  $T_B \gtrsim 100\hbar/v$ , the readout dot occupation shows a straight “fidelity plateau” at  $n_R = 1/2$ , which is consistent with the expectation that braiding induces a  $\pi/2$  rotation around the qubit  $z$  axis (see the “ $1 \times$  exchange” column in Table I). For intermediate braiding times, the occupation of the readout dot depends strongly on the actual value of the braiding time. Here the MZM exchange is slow enough to induce dynamics in the system, but the diabatic errors are significant.

One might wonder whether an average dot occupation of  $n_R = 1/2$  is a satisfying signature of a precisely functioning quantum gate? As we will see in Sec. IV, a similar result of  $n_R \approx 1/2$  arises also if the experiment is dominated by strong decoherence that randomizes the Majorana qubit during the exchange.

Hence we study, as an important control experiment, the case in which braiding consists of two consecutive counterclockwise exchanges of the MZMs ( $2 \times$  exchange). Our numerical simulation of this control experiment is shown in Fig. 3(b). Here the braiding time  $T_B$  incorporates both exchanges:  $T_B = 12N_c T_{\text{ramp}}$ . The behavior of the final readout-dot occupation for short and intermediate braiding times is similar to that seen in panel (a). However, in the adiabatic limit  $T_B \rightarrow \infty$ , the readout dot occupation is zero as anticipated, e.g., in the last column of the Table I.

One aspect of the topological protection of a Majorana qubit is that errors induced by the finite overlap of the MZMs can be exponentially suppressed by increasing the system size. Even though the simulations in Fig. 3 are not subject to such errors, we highlight an interesting and potentially useful aspect of chain length dependence here. The length dependence of the final-state readout dot occupation is shown in Fig. 4. Importantly, the horizontal axis shows the time  $T_{\text{ramp}}$  needed to move the topological-trivial domain wall by a single site, and not the complete braiding time  $T_B = 12N_c T_{\text{ramp}}$ . Our conclusion is that the results for the three different system sizes  $N_c \in \{1, 2, 3\}$  show very similar power-law-type behavior for intermediate times, which provides the clear prediction that this behavior is universal, and hence can be used to extrapolate for larger system sizes ( $N_c > 3$ ) as well. This result is analogous to our earlier result for braiding in the SSH model; see Fig. 3(b) of Ref. [74].

Note also that in Fig. 4, the apparent error of the gate, i.e., the final occupation of the readout dot, saturates for large ramp times at a plateau of  $n_R \approx 10^{-5}$ . This is a consequence of the nonprotected nature of the tunnel-pulse-based  $\pi/2$  gates and readout; errors caused by such tunnel-pulse-based operations set the height of this plateau. (See, e.g., Fig. 2 of [67])

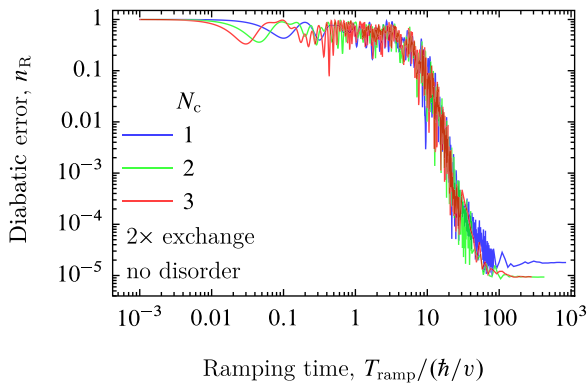


FIG. 4. Diabatic errors of the braiding-based  $\pi/2$  gate scale with the ramping time. Diabatic error is illustrated as a function of the ramping time in the case of the  $2\times$  exchange protocol, for three different chain lengths. For this protocol, diabatic error corresponds to the readout dot occupation at the end of the protocol. The three curves overlap, showing that the diabatic error scales with the ramping time (which is inversely proportional to the domain-wall speed), irrespective of the chain length. For longer ramping times  $T \gtrsim 100\hbar/v$ , the  $n_R$  curves saturate due to the nonzero error of tunnel-pulse-based gates and readout.

describing readout error in a similar readout scheme.) This is a feature that we expect to see in future braiding experiments as well.

#### IV. CHARGE NOISE INDUCES MAJORANA QUBIT DEPHASING IF BRAIDING IS SLOW

The braiding-based  $\pi/2$ -gate on the Majorana qubit is an example of a topological quantum gate: the operation on the qubit does not depend on the geometry of the path of control parameters, only on the topology of the path. This topological nature implies robustness, i.e., resilience to imperfections in the control path. We investigate this robustness here. As the imperfection, we focus on  $1/f$  charge noise, which is known to be an important ingredient in quantum dots [35,59–65], and hence is expected to be relevant in future Majorana qubit experiments based on quantum dot arrays as well.

Following earlier studies, we model  $1/f$  charge noise in our multidot system as *quasistatic disorder* [28,67]. We assume that we set our system in the topological fully dimerized limit, but there is also an unwanted, uncontrolled, and spatially uncorrelated random quasistatic contribution to each on-site energy (except to the potential of the readout dot, see below). These on-site energy contributions are represented as independent zero-mean Gaussian random variables:

$$\delta\mu_{n,i}, \delta\mu_k \sim \mathcal{N}(0, \sigma_\mu^2), \quad (8a)$$

$$\delta\mu_R = 0, \quad (8b)$$

where  $\sigma_\mu$  is the disorder strength, i.e., the standard deviation of the Gaussian distribution,  $n = \{1, 2, 3\}$ ,  $i = \{1, 2, \dots, N_c\}$ , and  $k = \{0, 1, 2, \dots, 2N_c + 1\}$ . Note that static disorder is a much studied ingredient of the Kitaev chain model; see, e.g., Refs. [29,75].

In the Ramsey-type protocol we consider in this work, a single data point (readout dot occupation) is obtained by

taking multiple runs of the very same experiment and averaging the binary values (0 or 1) of the readout dot charge measured upon the multiple runs. The assumption of the quasistatic model is that this averaging procedure is equivalent to averaging over the disorder configurations described by Eq. (8).

We focus on the effect of disorder on the braiding-based gates. Hence, we do not add disorder to the on-site energy of the readout dot, and we do not include imperfections in the tunnel pulses  $u_p(t)$  or  $u_R(t)$ . Such imperfections would in fact cause errors that are not suppressed by increasing system size  $N_c$ . In contrast, the on-site energy disorder (whose effects we describe below) and disorder in the static tunnel amplitudes and pair potentials (which we do not describe explicitly below) cause errors that are suppressed by increasing system size  $N_c$ .

Figure 5(a) shows the disorder-averaged result of the Ramsey-type protocol with  $1\times$  exchange, averaging  $N_r = 1000$  different disorder realizations for the disorder strength  $\sigma_\mu = 0.15v$ . We show results of simulations where the initial state is formed by the product of the even ground state of the  $Y$  junction, the even ground state of the wire, and the empty readout dot (see Appendix A for details). The quantity we plot in Fig. 5(a) is the disorder-averaged final readout dot occupation

$$\bar{n}_R = \frac{1}{N_r} \sum_{j=1}^{N_r} n_R^{(j)}, \quad (9)$$

where  $n_R^{(j)}$  is the expectation value of the final readout dot occupation for the  $j$ th disorder realization. (Note that these expectation values  $n_R^{(j)}$  are random variables themselves, since they depend on the disorder configuration.) Furthermore, the error bars show the 10–90 % quantiles of the 1000 different realizations.

Figure 5(a) shows that for short braiding times,  $T_B \lesssim 50\hbar/v$ , diabatic errors corrupt the gate. For intermediate times,  $50\hbar/v \lesssim T_B \lesssim 100\hbar/v$ , the readout dot occupation is close to the clean result  $n_R = 1/2$ , with small fluctuations as shown by the error bars. For long times,  $T_B \gtrsim 100\hbar/v$ , the readout dot occupation is still close to the clean result  $n_R = 1/2$ , but the fluctuations grow significantly.

The fluctuations seen for  $T_B \gtrsim 50\hbar/v$  in Fig. 5(a) are interpreted as dephasing occurring during the braiding-based quantum operation. The on-site energy disorder detunes the Kitaev chains from the fully dimerized limit, causing hybridization of MZMs and corresponding energy splittings, both in the  $Y$  junction and in the straight Kitaev wire. As a consequence of the splittings, the dynamical phases acquired by the Majorana qubit basis states become different, which in turn causes significant deviations from the ideal (disorder-free and adiabatic) scenario, which relies only on the geometric phase difference  $\pi/2$  between the even and odd ground states of the  $Y$  junction.

Although the increasing error bars with increasing braiding time, seen in Fig. 5(a) for  $T_B \gtrsim 50\hbar/v$ , provide a clear numerical signature of dephasing, these error bars cannot be revealed by an experiment that follows our protocol. The reason is as follows. The randomness of disorder implies that the final dot

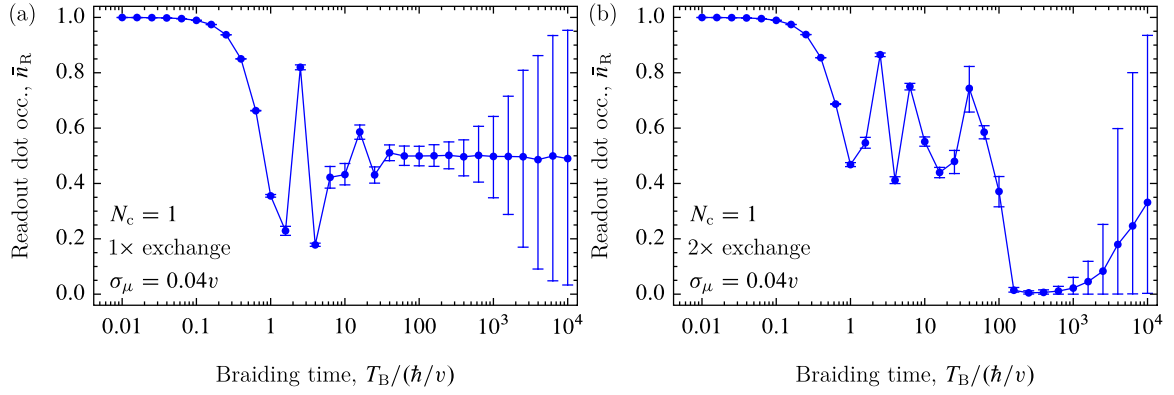


FIG. 5. Numerical simulation of the braiding experiment in the presence of on-site disorder. Disorder-averaged final-state occupation  $\bar{n}_R$  of the readout dot is shown as a function of the braiding time, for the smallest system size  $N_c = 1$  with disorder strength  $\sigma_\mu = 0.04v$ . Each curve is a result of  $N_f = 1000$  realizations, dots show the mean of the occupations, while error bars depict the 10–90 % quantiles. (a) Single exchange. Disorder-averaged readout dot occupation for long braiding time is similar to that without disorder [see Fig. 3(a)], but the error bars arise due to disorder. (b) Double exchange. The disorder changes the mean of the readout dot occupation in the adiabatic limit [cf. Fig. 3(b)], and the error bars also show the influence of disorder. The plateau between 100 and 1000 can serve as the signature of successful braiding in a real experiment.

occupation  $n_R$  itself is a random variable. However, in a single run of the experiment, say, the  $j$ th run, the charge readout result is either 0 or 1, with the probability of 1 determined by  $n_R^{(j)}$ . The data point for a given braiding time is the average of these binary results for a large number of runs with a fixed  $T_B$ . This averaging procedure yields the disorder-averaged  $\bar{n}_R$ , and the result carries no information about the disorder-induced fluctuations of  $n_R$ .

Nevertheless, dephasing during the braiding-based gate can be characterized by our protocol. This is done by doing the exchange twice. In that setting, the idealized readout dot occupation is  $n_R = 0$ , and dephasing causes deviations of the disorder-averaged  $\bar{n}_R$  from that value. Figure 5(b) shows the disorder-averaged result of the  $2\times$  exchange protocol, along with error bars as discussed above. For short braiding times  $T_B \lesssim 200\hbar/v$ , there is no significant difference from the clean case, and the result is dominated by diabatic error. For intermediate braiding times,  $200\hbar/v \lesssim T_B \lesssim 1000\hbar/v$ , a “fidelity plateau” is seen, which is the signature that each MZM exchange realizes a  $\pi/2$  gate. We anticipate that such fidelity plateaus will serve as important signatures of topologically protected quantum gates in future experiments. For longer braiding times,  $T_B \gtrsim 1000\hbar/v$ , the result is dominated by disorder-induced dephasing that happens during the MZM exchanges.

To illustrate the topological protection of the braiding-based quantum gate, we show how the fidelity plateau length varies if we vary the system size and the strength of the disorder. In Fig. 6(a), the disorder-averaged readout dot occupation  $\bar{n}_R$  is shown for the three smallest system sizes  $N_c = 1, 2, 3$  using the  $2\times$  exchange protocol. Disorder strength is set to  $\sigma_\mu = 0.15v$ , which is strong enough to reduce the occupation to a dip for  $N_c = 1$  (blue). By increasing the chain length to  $N_c = 2$  (green), a fidelity plateau is developed, which flattens further for an even larger system size  $N_c = 3$  (red). This improvement of the gate quality by increasing the system size will probably be used as a hallmark of topologically protected

quantum gates in future braiding experiments. In Fig. 6(b), we show the disorder-averaged readout dot occupation curves for different disorder strengths in the case of the smallest system size  $N_c = 1$ . The main observation here is that the fidelity plateau gets longer and more flat as disorder strength is decreased.

## V. DISCUSSION

### A. Experimental timescales

Here, we convert our numerical results discussed above to quantitative estimates of timescales for future experiments. Based on the recent experiment of Ref. [58], we assume an induced gap of  $30\mu\text{eV}$  in our fully dimerized Kitaev-chain model, equivalent to setting  $v = \Delta = 15\mu\text{eV}$ . The simplest quantum-dot-based braiding setup corresponds to our  $N_c = 1$  case, requiring eight quantum dots.

Assuming that our protocol will be realized experimentally in such a setup, we ask the following question: for which experimental result are we convinced that the experiment demonstrated a braiding-based topological quantum gate? That is, when do we say that a fidelity plateau is “long and flat” enough to be convincing evidence of such a gate? To make this question a bit more specific: what is the level of disorder that enables the experimenter to observe a fidelity plateau below the error level of 1% ( $\bar{n}_R \leq 0.01$ ) such that the fidelity plateau spreads over at least one order of magnitude along the braiding-time axis? Using the estimate  $v = \Delta = 15\mu\text{eV}$ , a quantitative answer can be read off Fig. 6(b): for  $\sigma_\mu = 0.02v = 0.3\mu\text{eV}$  (red squares), the fidelity plateau spreads in the range  $250\hbar/v \lesssim T_B \lesssim 2500\hbar/v$ , which is equivalent to  $5.5\text{ ns} \lesssim T_B \lesssim 55\text{ ns}$ .

We note that typical quantum dot devices show on-site energy fluctuations ( $\sigma_\mu$ ) of the order of a few microelectronvolts; see, e.g., the experimental data listed in Table II of Ref. [18]. However, in recent state-of-the-art experiments with a double quantum dot,  $\sigma_\mu \sim 0.1\mu\text{eV}$  has been achieved [76]. Even though it is a highly nontrivial technological challenge

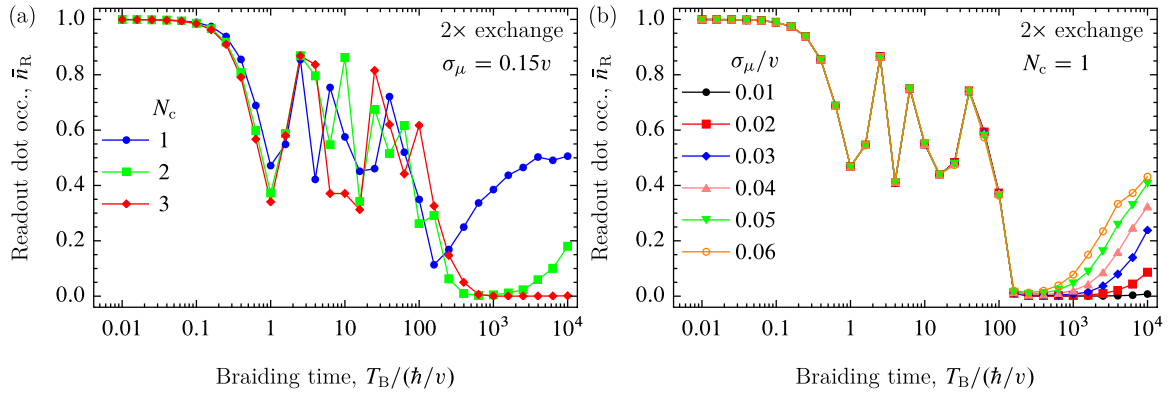


FIG. 6. Demonstration of topological protection. Disorder-averaged occupation of the readout dot as a function of the braiding time is shown in the double-exchange protocol (a) for a given disorder strength  $\sigma_\mu = 0.15v$  and for different system sizes; (b) for the smallest system size  $N_c = 1$  and for different disorder strengths. Each curve is obtained by averaging for  $N_r = 1000$  realizations. For (a) increasing system size, and (b) for decreasing disorder strength, a plateau with  $\bar{n}_R \approx 0$  appears for long braiding times, and the plateau length increases.

to combine the high-quality dot structures with superconductors, these numbers give hope that topological quantum gates can be experimentally demonstrated using small quantum dot arrays.

### B. Beyond the minimal model

The model we have used in this work is a minimal one, allowing us to focus on a few key physical ingredients, and to highlight a few mechanisms likely to affect the proposed experiment. Here, we list further ingredients that are worthwhile to incorporate in future studies.

(i) *Modeling braiding dynamics with a microscopic dot-array Hamiltonian.* We have assumed that the Kitaev chain model provides a faithful description of a quantum dot array proximitized by superconductors. Much physical insight behind that assumption has been provided by Refs. [50–52,66]. However, it will be an interesting and relevant extension of our work to study the braiding-induced dynamics in a more realistic dot array model, where, e.g., Zeeman sublevels of the dots, excited orbitals, Coulomb repulsion, spin-orbit interaction, etc., are explicitly incorporated. The more realistic character of such models will imply, e.g., an increased MZM hybridization with respect to the dimerized limit of the Kitaev chain model, and in turn, a greater susceptibility of the Majorana qubit to charge noise.

(ii) *Role of fluctuations of  $v$  and  $\Delta$ .* We have assumed that the static tunnel amplitudes ( $v$ ) and pair potentials ( $\Delta$ ) are perfectly controlled. In an experiment, this is not the case. For small quantum dot arrays, the effect of their fluctuations can be relevant. For example, the MZM energy splitting of a two-site Kitaev chain is linear in the parameter  $|v| - |\Delta|$  (see Ref. [66]), hence the fluctuations of  $v$  and  $\Delta$  can cause significant dephasing. Note that this dephasing mechanism is suppressed exponentially by increasing the system size, similar to the case of on-site energy fluctuations we studied above.

For semiconductor quantum dots, it has been experimentally established that charge noise affects the on-site energies much more than the interdot tunneling energies. This has been

revealed in a number of experiments [77–79] implementing the Loss-DiVincenzo two-qubit gate in a double quantum dot. In those experiments, the charge noise had the weakest effect when the on-site energies are tuned to be identical (“symmetric operation point”). In that operation point, charge noise induces decoherence via the tunneling amplitude, whereas away from that point, charge noise induces decoherence via the on-site energy detuning. Therefore, the symmetric point being the sweet spot indicates that the main effect of charge noise is the on-site detuning fluctuation. This was a further motivation to focus on on-site energy fluctuations in the present paper, and postpone the study of tunneling energy fluctuations for future work.

(iii) *Errors in the tunnel pulses.* A further difference between our minimal model and experiments is that in the latter, the tunnel pulses are imperfect; e.g., pulse duration, pulse amplitude, and pulse shape deviate from ideal. Such perturbations, if strong enough, could significantly reduce the quality (flatness and length) of the fidelity plateaus shown in Figs. 5(b) and 6.

For semiconductor quantum dot spin qubits, the experimentally most relevant noise sources are hyperfine noise, charge noise, and electron-phonon interaction (see, e.g., Sec. VI of [80]). Errors caused by pulse imperfections might also be relevant, but those have not obstructed beyond-99% gate fidelities [61], hence we consider them as a secondary threat for Majorana qubits as well, and we postpone studying them to future work.

(iv) *On-site energy fluctuations of the readout dot.* In this study, we have disregarded on-site energy fluctuations of the readout dot to focus on the features of MZM braiding. Such fluctuations lead to readout error [67], which, similarly to the effect of tunnel pulse errors, reduces the quality of the fidelity plateaus. Based on our earlier results [67], we estimate that extending the on-site energy fluctuations to the readout dot would not change the quantitative timescale analysis of Sec. V A.

(v) *Beyond the quasistatic approximation.* In this work, we use the quasistatic approximation [81,82] to describe the effect of charge noise. In real devices, charge noise often

exhibits an  $1/f$ -type spectrum [18,35,60–65,73,83,84]. Incorporating the  $1/f$  frequency dependence of noise in our model, following, e.g., Refs. [19,35,73,83], could be an important addition to the present work.

(vi) *Qubit initialization.* Above, we assumed that the Majorana qubit can be initialized to a particular state of the fourfold-degenerate ground-state manifold. One way to achieve this experimentally is via thermalization. The experimenter can tune both the  $Y$  junction and the straight wire away from the fully dimerized limit to open up an energy splitting between the even and odd ground states of both subsystems, and to make the ground state unique (e.g.,  $|e, e\rangle$ ). Then, thermalization will relax the system to this unique ground state, completing the initialization step.

(vii) *Thermalization-induced decoherence during braiding.* In our simulations above, we neglect effects and errors induced by the finite-temperature bath that is unavoidably present in a real experiment. This effect is discussed in detail in Ref. [23], using a Kitaev-chain model similar to ours. For a simple numerical estimate based on the parameters of Sec. V A, we assume that the thermalizing bath cannot change the fermion number parity of the multidot setup during the braiding phase. For that case, we estimate the error due to thermalization as the probability of having excitation energy  $2v$  in thermal equilibrium. This error has no significant effect on the fidelity plateau defined by  $n_R \leq 0.01$  if  $e^{-2v/k_B T} \leq 0.01$ , which is converted to the condition  $T \leq 76$  mK for  $v = 15$   $\mu$ eV as assumed in Sec. V A. Such temperatures are achieved in dilution refrigerators.

(viii) *Nuclear spins and spin-orbit interaction.* To build a Kitaev chain type system from quantum dots, it is essential to break time-reversal symmetry by a substantial Zeeman field [2,49–51]. In line with that, each on-site orbital of the Kitaev chain model corresponds to a single Zeeman sublevel. Hyperfine interaction does add low-frequency noise to the energies of these Zeeman sublevels. The strength of this noise can be estimated from earlier results on semiconductor spin qubits. In III-V semiconductors, where hyperfine effects are very significant, the hyperfine noise strength of an electronic Zeeman sublevel is of the order of 1 millitesla, or 60 nanoelectronvolts [85]. This is much less than the typical charge noise level in quantum dots, of the order of microelectronvolts, which we have taken into account in our simulations above. Hence, it is a reasonable approximation to neglect hyperfine noise, as it has a weaker effect than charge noise. We also note that spin-orbit interaction can act as a dominant decoherence mechanism in semiconductor quantum dot spin qubits; however, it becomes a source of decoherence only when it is combined with charge noise. Therefore, spin-orbit induced decoherence is a secondary effect of charge noise, and hence we expect that this secondary effect is dominated by the primary effect of charge noise, which we include in our simulations discussed above.

(ix) *Optimal control.* In our numerical simulation, excited states are populated due to faster-than-adiabatic control. These excitations cause deviations, seen for short braiding times, from the idealized results  $n_R = 1/2$  [Figs. 3(a) and 5(a)] and  $n_R = 0$  [Figs. 3(b), 4, 5(b), and 6]. These diabatic errors could be reduced, e.g., by quantum optimal control tools [86]. An example of a theoretical study is [41]. Based on the history of solid-state qubits (superconducting

circuits and semiconductor quantum dots), we expect that the first generation of Majorana qubit experiments will attempt to demonstrate initialization, control, and readout without optimal-control techniques, and once these functionalities have been demonstrated, then second-generation experiments will utilize optimal control theory.

(x) *Open-system approaches.* It is possible to add open-system dynamics to the model considered here, to describe further decoherence mechanisms. This has been done, e.g., in Ref. [23], using a Markovian framework. We note that an open-system approach to numerical simulations of braiding does not scale as favorably as our approach based on the BdG technique. For example, by adding a bosonic bath to the few-site superconducting model, as in Eq. (20) of Ref. [23], the Hamiltonian loses its quadratic character (in particle creation-annihilation operators), and hence the economical BdG approach cannot be used to simulate the dynamics. In the case of an  $N$ -site model, the BdG matrix has a linear dimension of  $2N$ , which is linear in  $N$ ; however, the even and odd Fock space each has dimension  $2(N - 1)$ , which is exponential in  $N$ . The latter exponential scaling quickly becomes prohibitive for numerical simulations.

(xi) *Variations of our braiding scheme.* Our Ramsey-type braiding experiment outlined in Figs. 1 and 2 involves two nonprotected gates that rotate the qubit by angle  $\pi/2$ . In an experiment, it is possible to change those rotation angles continuously, and measure the readout dot final occupation as a function of those two angle parameters; i.e., those angles can be used as control knobs. We expect that the earliest braiding experiments will not be able to produce the fidelity plateaus we obtain in our simulations; however, the comparison of experiments and simulations exploring the rotation angle dependence of the readout dot occupation can be used to identify the error mechanisms leading to the loss of fidelity.

An alternative of our setup in Fig. 1, which does not require nonprotected qubit rotations, is where the middle two Majorana zero modes are coupled by a  $Y$  junction. In that setup, the nonprotected gates can be substituted by braiding in the latter  $Y$  junction. However, that setup requires *two*  $Y$  junctions to function properly, as opposed to the *single*  $Y$  junction setup of Fig. 1. Since nonprotected qubit rotations based on simple tunnel pulses have already been demonstrated with, e.g., semiconductor spin qubits, we find our single- $Y$ -junction setup more feasible and easier to realize.

## VI. CONCLUSIONS

In conclusion, we have proposed a setup and a protocol for experimental demonstration of a braiding-based  $\pi/2$  gate on a Majorana qubit. The protocol is based on a proximitized quantum-dot array, and it is composed of auxiliary (nontopological) quantum gates, a braiding-based topological quantum gate, and qubit readout via parity-to-charge conversion and charge measurement. We focused on the effect of charge noise, which we incorporate in our simulations as quasistatic on-site disorder. Our results confirm that the braiding-based gate suffers from diabatic errors for short braiding times, and they demonstrate noise-induced dephasing for long braiding times. For intermediate times, a fidelity plateau can develop, which is made flatter and longer if disorder strength is

decreased or if system size is increased. Our numerical results provide quantitative predictions for the quality of future braiding experiments, which can hopefully be built by combining today's state-of-the-art quantum dot arrays and proximity-induced superconductivity.

### ACKNOWLEDGMENTS

We thank J. Asbóth, G. Széchenyi, and members of the Kouwenhoven group for useful and encouraging discussions. This research was supported by the Ministry of Culture and Innovation and the National Research, Development and Innovation Office (NKFIH) within the Quantum Information National Laboratory of Hungary (Grant No. 2022-2.1.1-NL-2022-00004), by the NKFIH via the OTKA Grant No. 132146, and by the European Union within the Horizon Europe research and innovation programme via the Project No. 101069515 (IGNITE).

### APPENDIX: BOGOLIUBOV-DE GENNES FORMALISM FOR DYNAMICS

Our numerical results in the main text are obtained by applying the BdG formalism. Here we outline how to calculate the time dependence of the readout dot occupation via

$$n_R(t) = \langle \Psi(t) | c_R^\dagger c_R | \Psi(t) \rangle, \quad (\text{A1})$$

where  $|\Psi(t)\rangle$  is the time-evolved many-body state developing from the initial state  $|\Psi_i\rangle$  of the system.

The time-dependent Fock-space Hamiltonian in Eq. (4) describes the time evolution of the system. To construct the BdG Hamiltonian, we define the vector of the local fermionic operators

$$\tilde{\mathbf{c}} = \begin{pmatrix} \mathbf{c}_Y \\ \mathbf{c}_Y^\dagger \\ \mathbf{c}_W \\ \mathbf{c}_W^\dagger \\ c_R \\ c_R^\dagger \end{pmatrix}, \quad (\text{A2})$$

where  $\mathbf{c}_Y$  and  $\mathbf{c}_W$  denote the vector of annihilation operators of the  $Y$  junction and the straight wire, respectively. Using the vector  $\tilde{\mathbf{c}}$ , we can rewrite the Hamiltonian as

$$H(t) = \frac{1}{2} \tilde{\mathbf{c}}^\dagger \mathcal{H}(t) \tilde{\mathbf{c}} + \frac{1}{2} \sum_{i \in L} \mu_i, \quad (\text{A3})$$

where  $\mathcal{H}(t)$  is the BdG Hamiltonian, and  $L$  is the set of all site labels.

At  $t = 0$ , the system is decoupled to three components ( $Y$  junction, straight wire, readout dot) by setting  $u_R(0) = u_P(0) = 0$ , and hence the BdG Hamiltonian has the form

$$\mathcal{H}(0) = \begin{pmatrix} \mathcal{H}_Y(0) & 0 & 0 \\ 0 & \mathcal{H}_W(0) & 0 \\ 0 & 0 & \mathcal{H}_R(0) \end{pmatrix}, \quad (\text{A4})$$

where  $\mathcal{H}_Y(0)$ ,  $\mathcal{H}_W(0)$ , and  $\mathcal{H}_R(0)$  are the BdG Hamiltonian of the  $Y$  junction, the straight wire, and the readout dot, at  $t = 0$ , respectively.

As usual in the BdG formalism, we use a time-dependent BdG Hamiltonian that is particle-hole symmetric for all times  $t$ :

$$\mathcal{P} \mathcal{H}(t) \mathcal{P}^{-1} = -\mathcal{H}(t). \quad (\text{A5})$$

Here, the particle-hole transformation reads

$$\mathcal{P} = \begin{pmatrix} \sigma_x \otimes \mathbb{1}_{N_Y} & 0 & 0 \\ 0 & \sigma_x \otimes \mathbb{1}_{N_W} & 0 \\ 0 & 0 & \sigma_x \end{pmatrix} K, \quad (\text{A6})$$

where  $\sigma_x$  is the first Pauli matrix acting on the Nambu (particle-hole) degree of freedom,  $\mathbb{1}_n$  is the  $n \times n$  identity matrix,  $N_Y$  ( $N_W$ ) is the number of the sites in the  $Y$  junction (straight wire), and  $K$  is complex conjugation. We note that each of the three subsystems alone has particle-hole symmetry.

Our goal is to describe the expectation value of the readout dot occupation  $c_R^\dagger c_R$  at the final moment of the protocol. To this end, we first solve (numerically) the eigenvalue problem of the initial BdG Hamiltonians,  $\mathcal{H}_Y(0)$ ,  $\mathcal{H}_W(0)$ , and  $\mathcal{H}_R(0)$ , we find the eigenvalues of the subsystems  $\lambda_{Y,i}$ ,  $\lambda_{W,i}$ , and  $\lambda_{R,i}$ , as well as the corresponding eigenvectors  $\phi_{Y,i}$ ,  $\phi_{W,i}$ , and  $\phi_{R,i}$ , where  $i = 1, 2, \dots, 2N_k$ ,  $N_k$  is the number of sites in the given subsystem, and  $k \in \{Y, W, R\}$  denotes the subsystem. We order the eigenvalues such that  $\lambda_{k,i} \geq 0$  and  $\lambda_{k,i+N} = -\lambda_{k,i}$  for  $1 \leq i \leq N \equiv N_Y + N_W + N_R$ . Furthermore, we choose the eigenvectors such that  $\phi_{k,i+N} = \mathcal{P} \phi_{k,i}$ .

With the eigenvectors  $\phi_{k,i}$  at hand, we can express the unitary matrix  $U'$  that diagonalizes  $\mathcal{H}(0)$ :

$$U' = \begin{pmatrix} U_Y & 0 & 0 \\ 0 & U_W & 0 \\ 0 & 0 & U_R \end{pmatrix}, \quad (\text{A7})$$

where  $U_Y$ ,  $U_W$ , and  $U_R$  are the diagonalizers of the  $Y$  junction, the straight wire, and the readout dot, respectively. The diagonalizer of subsystem  $k \in \{Y, W, R\}$  can be written as

$$U_k = \begin{pmatrix} \phi_{k,1}^\dagger \\ \vdots \\ \phi_{k,2N_k}^\dagger \end{pmatrix}. \quad (\text{A8})$$

The vector of quasiparticle operators can be expressed as

$$\tilde{\mathbf{d}}' = U' \tilde{\mathbf{c}} = \begin{pmatrix} \mathbf{d}_Y \\ \mathbf{d}_Y^\dagger \\ \mathbf{d}_W \\ \mathbf{d}_W^\dagger \\ d_R \\ d_R^\dagger \end{pmatrix}, \quad (\text{A9})$$

where  $\mathbf{d}_Y$ ,  $\mathbf{d}_W$ , and  $d_R$  are the quasiparticle operators corresponding to the  $Y$  junction, the straight wire, and the readout dot, respectively. The fact that the on-site energy of the readout dot is zero leaves  $d_R$  ambiguous; for concreteness, we define  $d_R = c_R$ .

To highlight the special role of the quasi-zero-energy excitations, we reorder the vector of quasiparticle operations

as

$$\tilde{\mathbf{d}} = \underbrace{\Pi U'}_U \tilde{\mathbf{c}} = \begin{pmatrix} d_1 \\ \dots \\ d_N \\ d_1^\dagger \\ \dots \\ d_N^\dagger \end{pmatrix}, \quad (\text{A10})$$

where  $d_1$  ( $d_2$ ) corresponds to the quasi-zero-energy excitation of the  $Y$  junction (straight wire),  $d_i$  ( $i = 3, \dots, N$ ) are ordered such a way that the corresponding excitation energies are in ascending order, furthermore  $\Pi$  is the permutation matrix corresponding to the reordering.

As stated above, our goal is to compute the time dependence of the readout dot occupation via Eq. (A1), which we rephrase as

$$n_R(t) = \langle \Psi_i | [\tilde{\mathbf{c}}(t)]_{2N} [\tilde{\mathbf{c}}(t)]_{2N-1} | \Psi_i \rangle, \quad (\text{A11})$$

where  $[\dots]_j$  denotes the  $j$ th component of the vector,  $|\Psi_i\rangle$  is a given initial state of the system, and the elements of the vector  $\tilde{\mathbf{c}}(t)$  are the elements of the vector  $\tilde{\mathbf{c}}$ , transformed to the Heisenberg picture:

$$\tilde{\mathbf{c}}(t) = \underbrace{\mathcal{T} e^{-\frac{i}{\hbar} \int_0^t \mathcal{H}(\tau) d\tau}}_{\mathcal{U}(t)} \tilde{\mathbf{c}}, \quad (\text{A12})$$

where  $\mathcal{T}$  is the time ordering operator and  $\mathcal{U}(t)$  is the BdG propagator. Inserting Eq. (A12) into Eq. (A11) and using Eq. (A10), we obtain

$$\begin{aligned} n_R(t) &= \langle \Psi_i | [\mathcal{U} U^\dagger \tilde{\mathbf{d}}]_{2N} [\mathcal{U} U^\dagger \tilde{\mathbf{d}}]_N | \Psi_i \rangle \\ &= \sum_{n,m=1}^{2N} S_{nm}(t) \langle \Psi_i | \tilde{d}_n \tilde{d}_m | \Psi_i \rangle, \end{aligned} \quad (\text{A13})$$

where the second line is an implicit definition of

$$S_{nm}(t) = [\mathcal{U} U^\dagger]_{2N,n} [\mathcal{U} U^\dagger]_{N,m}. \quad (\text{A14})$$

In the main text, we focus on the case when  $|\Psi_i\rangle = |e, e, 0\rangle$ , i.e., both the  $Y$  junction and the straight wire are in its even ground state, and the readout dot is empty. The even-parity state could be the actual ground state (denoted by ‘‘G’’) or the first excited state (within the quasidegenerate ground-state subspace, denoted by ‘‘E’’) depending on the actual on-site energy disorder realization. The two states are related as

$$|E, G, 0\rangle = d_1^\dagger |G, G, 0\rangle, \quad (\text{A15a})$$

$$|G, E, 0\rangle = d_2^\dagger |G, G, 0\rangle. \quad (\text{A15b})$$

The readout dot occupation can be calculated for all four initial energy eigenstates  $|G, G, 0\rangle$ ,  $|E, G, 0\rangle$ ,  $|G, E, 0\rangle$ , and  $|E, E, 0\rangle$ . Evaluation of the matrix element of  $\langle \Psi_i | \tilde{d}_n \tilde{d}_m | \Psi_i \rangle$  in these four cases yields

$$n_R(t) \Big|_{|\Psi_i\rangle=|G,G,0\rangle} = \sum_{\mu=1}^N S_{\mu,N+\mu}(t), \quad (\text{A16a})$$

$$n_R(t) \Big|_{|\Psi_i\rangle=|E,G,0\rangle} = S_{N+1,1}(t) + \sum_{\mu=2}^N S_{\mu,N+\mu}(t), \quad (\text{A16b})$$

$$n_R(t) \Big|_{|\Psi_i\rangle=|G,E,0\rangle} = S_{N+2,2}(t) + \sum_{\mu\in\{1,3,4,\dots,N\}} S_{\mu,N+\mu}(t), \quad (\text{A16c})$$

$$\begin{aligned} n_R(t) \Big|_{|\Psi_i\rangle=|E,E,0\rangle} &= S_{N+1,1}(t) + S_{N+2,2}(t) \\ &+ \sum_{\mu=3}^N S_{\mu,N+\mu}(t). \end{aligned} \quad (\text{A16d})$$

To determine which case corresponds to the initial state  $|e, e, 0\rangle$ , we use the relation that

$$\det(U_Y) = \begin{cases} 1 & \text{if the actual ground state is even,} \\ -1 & \text{if the actual ground state is odd,} \end{cases} \quad (\text{A17})$$

and the corresponding relation for  $U_W$ .

Applying Eq. (A17) for the  $Y$  junction and for the straight wire, the state  $|e, e, 0\rangle$  can be identified as

$$|e, e, 0\rangle = \begin{cases} |G, G, 0\rangle & \text{if } \det(U_Y) = \det(U_W) = 1, \\ |E, G, 0\rangle & \text{if } -\det(U_Y) = \det(U_W) = 1, \\ |G, E, 0\rangle & \text{if } \det(U_Y) = -\det(U_W) = 1, \\ |E, E, 0\rangle & \text{if } \det(U_Y) = \det(U_W) = -1. \end{cases} \quad (\text{A18})$$

We note that if the on-site energy of the readout dot is zero, or if the on-site disorder is absent in the Kitaev chains, then there is at least one excitation with exactly zero energy. This leads to the degeneracy of the zero eigenvalue of  $\mathcal{H}_Y(0)$ ,  $\mathcal{H}_W(0)$ , and  $\mathcal{H}_R(0)$ . In turn, this leads to an ambiguity in constructing the matrices  $U_Y$ ,  $U_W$ , and  $U_R$ . We have already fixed the ambiguity of  $U_R$  after Eq. (A9). Regarding the  $Y$ -junction and straight wire, hosting Majoranas, care must be taken to use *fermionic* zero modes when assembling  $U_Y$  and  $U_W$ . Then, Eq. (A18) can be used to identify  $|e, e, 0\rangle$ .

- [1] D. A. Ivanov, Non-Abelian statistics of half-quantum vortices in  $p$ -wave superconductors, *Phys. Rev. Lett.* **86**, 268 (2001).
- [2] A. Y. Kitaev, Unpaired Majorana fermions in quantum wires, *Phys. Usp.* **44**, 131 (2001).
- [3] J. Alicea, Y. Oreg, G. Refael, F. von Oppen, and M. P. A. Fisher, Non-Abelian statistics and topological quantum information processing in 1D wire networks, *Nat. Phys.* **7**, 412 (2011).

- [4] V. Mourik, K. Zuo, S. M. Frolov, S. R. Plissard, E. P. A. M. Bakkers, and L. P. Kouwenhoven, Signatures of Majorana fermions in hybrid superconductor-semiconductor nanowire devices, *Science* **336**, 1003 (2012).
- [5] S. M. Albrecht, A. P. Higginbotham, M. Madsen, F. Kuemmeth, T. S. Jespersen, J. Nygård, P. Krogstrup, and C. M. Marcus, Exponential protection of zero modes in Majorana islands, *Nature (London)* **531**, 206 (2016).

- [6] J. Alicea, New directions in the pursuit of Majorana fermions in solid state systems, *Rep. Prog. Phys.* **75**, 076501 (2012).
- [7] C. W. J. Beenakker, Random-matrix theory of Majorana fermions and topological superconductors, *Rev. Mod. Phys.* **87**, 1037 (2015).
- [8] S. D. Sarma, M. Freedman, and C. Nayak, Majorana zero modes and topological quantum computation, *npj Quantum Inf.* **1**, 15001 (2015).
- [9] C. Beenakker and L. Kouwenhoven, A road to reality with topological superconductors, *Nat. Phys.* **12**, 618 (2016).
- [10] R. Aguado, Majorana quasiparticles in condensed matter, *Riv. Nuovo. Cim.* **40**, 523 (2017).
- [11] R. M. Lutchyn, E. P. A. M. Bakkers, L. P. Kouwenhoven, P. Krogstrup, C. M. Marcus, and Y. Oreg, Majorana zero modes in superconductor–semiconductor heterostructures, *Nat. Rev. Mater.* **3**, 52 (2018).
- [12] C. W. J. Beenakker, Search for non-Abelian Majorana braiding statistics in superconductors, *SciPost Phys. Lect. Notes* **15** (2020).
- [13] E. Prada, P. San-Jose, M. W. A. de Moor, A. Geresdi, E. J. H. Lee, J. Klinovaja, D. Loss, J. Nygård, R. Aguado, and L. P. Kouwenhoven, From Andreev to Majorana bound states in hybrid superconductor–semiconductor nanowires, *Nat. Rev. Phys.* **2**, 575 (2020).
- [14] M. S. Scheurer and A. Shnirman, Nonadiabatic processes in Majorana qubit systems, *Phys. Rev. B* **88**, 064515 (2013).
- [15] P. P. Aseev, J. Klinovaja, and D. Loss, Lifetime of Majorana qubits in Rashba nanowires with nonuniform chemical potential, *Phys. Rev. B* **98**, 155414 (2018).
- [16] P. P. Aseev, P. Marra, P. Stano, J. Klinovaja, and D. Loss, Degeneracy lifting of Majorana bound states due to electron-phonon interactions, *Phys. Rev. B* **99**, 205435 (2019).
- [17] J. C. Budich, S. Walter, and B. Trauzettel, Failure of protection of Majorana based qubits against decoherence, *Phys. Rev. B* **85**, 121405(R) (2012).
- [18] C. Knapp, T. Karzig, R. M. Lutchyn, and C. Nayak, Dephasing of Majorana-based qubits, *Phys. Rev. B* **97**, 125404 (2018).
- [19] D. Aasen, M. Hell, R. V. Mishmash, A. Higginbotham, J. Danon, M. Leijnse, T. S. Jespersen, J. A. Folk, C. M. Marcus, K. Flensberg, and J. Alicea, Milestones toward Majorana-based quantum computing, *Phys. Rev. X* **6**, 031016 (2016).
- [20] T. Karzig, C. Knapp, R. M. Lutchyn, P. Bonderson, M. B. Hastings, C. Nayak, J. Alicea, K. Flensberg, S. Plugge, Y. Oreg, C. M. Marcus, and M. H. Freedman, Scalable designs for quasiparticle-poisoning-protected topological quantum computation with Majorana zero modes, *Phys. Rev. B* **95**, 235305 (2017).
- [21] M. Hell, J. Danon, K. Flensberg, and M. Leijnse, Time scales for Majorana manipulation using Coulomb blockade in gate-controlled superconducting nanowires, *Phys. Rev. B* **94**, 035424 (2016).
- [22] A. Rahmani, B. Seradjeh, and M. Franz, Optimal diabatic dynamics of Majorana-based quantum gates, *Phys. Rev. B* **96**, 075158 (2017).
- [23] N. Breckwoldt, T. Posske, and M. Thorwart, Bath-induced decoherence in finite-size Majorana wires at non-zero temperature, *New J. Phys.* **24**, 013033 (2022).
- [24] B. Bauer, T. Karzig, R. V. Mishmash, A. E. Antipov, and J. Alicea, Dynamics of Majorana-based qubits operated with an array of tunable gates, *SciPost Phys.* **5**, 004 (2018).
- [25] I. C. Fulga, B. van Heck, M. Burrello, and T. Hyart, Effects of disorder on Coulomb-assisted braiding of Majorana zero modes, *Phys. Rev. B* **88**, 155435 (2013).
- [26] Z.-T. Zhang, F. Mei, X.-G. Meng, B.-L. Liang, and Z.-S. Yang, Effects of decoherence on diabatic errors in Majorana braiding, *Phys. Rev. A* **100**, 012324 (2019).
- [27] V. Kornich, X. Huang, E. Repin, and Y. V. Nazarov, Braiding and all quantum operations with Majorana modes in 1D, *Phys. Rev. Lett.* **126**, 117701 (2021).
- [28] P. Boross and A. Pályi, Dephasing of Majorana qubits due to quasistatic disorder, *Phys. Rev. B* **105**, 035413 (2022).
- [29] P. W. Brouwer, M. Duckheim, A. Romito, and F. von Oppen, Probability distribution of Majorana end-state energies in disordered wires, *Phys. Rev. Lett.* **107**, 196804 (2011).
- [30] G. Goldstein and C. Chamon, Decay rates for topological memories encoded with Majorana fermions, *Phys. Rev. B* **84**, 205109 (2011).
- [31] M. J. Schmidt, D. Rainis, and D. Loss, Decoherence of Majorana qubits by noisy gates, *Phys. Rev. B* **86**, 085414 (2012).
- [32] D. Rainis and D. Loss, Majorana qubit decoherence by quasiparticle poisoning, *Phys. Rev. B* **85**, 174533 (2012).
- [33] F. L. Pedrocchi and D. P. DiVincenzo, Majorana braiding with thermal noise, *Phys. Rev. Lett.* **115**, 120402 (2015).
- [34] H.-L. Lai, P.-Y. Yang, Y.-W. Huang, and W.-M. Zhang, Exact master equation and non-Markovian decoherence dynamics of Majorana zero modes under gate-induced charge fluctuations, *Phys. Rev. B* **97**, 054508 (2018).
- [35] R. V. Mishmash, B. Bauer, F. von Oppen, and J. Alicea, Dephasing and leakage dynamics of noisy Majorana-based qubits: Topological versus Andreev, *Phys. Rev. B* **101**, 075404 (2020).
- [36] C. Tutschku, R. W. Reithaler, C. Lei, A. H. MacDonald, and E. M. Hankiewicz, Majorana-based quantum computing in nanowire devices, *Phys. Rev. B* **102**, 125407 (2020).
- [37] O. Zilberberg, B. Braunecker, and D. Loss, Controlled-NOT gate for multiparticle qubits and topological quantum computation based on parity measurements, *Phys. Rev. A* **77**, 012327 (2008).
- [38] C. W. J. Beenakker, D. P. DiVincenzo, C. Emary, and M. Kindermann, Charge detection enables free-electron quantum computation, *Phys. Rev. Lett.* **93**, 020501 (2004).
- [39] S. Vijay and L. Fu, Teleportation-based quantum information processing with Majorana zero modes, *Phys. Rev. B* **94**, 235446 (2016).
- [40] S. Plugge, A. Rasmussen, R. Egger, and K. Flensberg, Majorana box qubits, *New J. Phys.* **19**, 012001 (2017).
- [41] T. Karzig, F. Pientka, G. Refael, and F. von Oppen, Shortcuts to non-Abelian braiding, *Phys. Rev. B* **91**, 201102(R) (2015).
- [42] C. Knapp, M. Zaletel, D. E. Liu, M. Cheng, P. Bonderson, and C. Nayak, The nature and correction of diabatic errors in anyon braiding, *Phys. Rev. X* **6**, 041003 (2016).
- [43] A. Nag and J. D. Sau, Diabatic errors in Majorana braiding with bosonic bath, *Phys. Rev. B* **100**, 014511 (2019).
- [44] J. P. T. Stenger, N. T. Bronn, D. J. Egger, and D. Pekker, Simulating the dynamics of braiding of Majorana zero modes using an IBM quantum computer, *Phys. Rev. Res.* **3**, 033171 (2021).
- [45] C. S. Amorim, K. Ebihara, A. Yamakage, Y. Tanaka, and M. Sato, Majorana braiding dynamics in nanowires, *Phys. Rev. B* **91**, 174305 (2015).

- [46] Q.-B. Cheng, J. He, and S.-P. Kou, Verifying non-Abelian statistics by numerical braiding Majorana fermions, *Phys. Lett. A* **380**, 779 (2016).
- [47] M. Sekania, S. Plugge, M. Greiter, R. Thomale, and P. Schmitteckert, Braiding errors in interacting Majorana quantum wires, *Phys. Rev. B* **96**, 094307 (2017).
- [48] F. Harper, A. Pushp, and R. Roy, Majorana braiding in realistic nanowire Y-junctions and tuning forks, *Phys. Rev. Res.* **1**, 033207 (2019).
- [49] M. Leijnse and K. Flensberg, Parity qubits and poor man's Majorana bound states in double quantum dots, *Phys. Rev. B* **86**, 134528 (2012).
- [50] J. D. Sau and S. D. Sarma, Realizing a robust practical Majorana chain in a quantum-dot-superconductor linear array, *Nat. Commun.* **3**, 964 (2012).
- [51] I. C. Fulga, A. Haim, A. R. Akhmerov, and Y. Oreg, Adaptive tuning of Majorana fermions in a quantum dot chain, *New J. Phys.* **15**, 045020 (2013).
- [52] A. Tsintzis, R. S. Souto, and M. Leijnse, Creating and detecting poor man's Majorana bound states in interacting quantum dots, *Phys. Rev. B* **106**, L201404 (2022).
- [53] C.-X. Liu, G. Wang, T. Dvir, and M. Wimmer, Tunable superconducting coupling of quantum dots via andreev bound states in semiconductor-superconductor nanowires, *Phys. Rev. Lett.* **129**, 267701 (2022).
- [54] A. R. Mills, D. M. Zajac, M. J. Gullans, F. J. Schupp, T. M. Hazard, and J. R. Petta, Shuttling a single charge across a one-dimensional array of silicon quantum dots, *Nat. Commun.* **10**, 1063 (2019).
- [55] S. G. J. Philips, M. T. Mađzik, S. V. Amitonov, S. L. de Snoo, M. Russ, N. Kalhor, C. Volk, W. I. L. Lawrie, D. Brousse, L. Tryputen, B. P. Wuetz, A. Sammak, M. Veldhorst, G. Scappucci, and L. M. K. Vandersypen, Universal control of a six-qubit quantum processor in silicon, *Nature* **609**, 919 (2022).
- [56] A. J. Weinstein, M. D. Reed, A. M. Jones, R. W. Andrews, D. Barnes, J. Z. Blumoff, L. E. Euliss, K. Eng, B. H. Fong, S. D. Ha, D. R. Hulbert, C. A. C. Jackson, M. Jura, T. E. Keating, J. Kerckhoff, A. A. Kiselev, J. Matten, G. Sabbir, A. Smith, J. Wright *et al.*, Universal logic with encoded spin qubits in silicon, *Nature (London)* **615**, 817 (2023).
- [57] H. Wu, P. Zhang, J. P. T. Stenger, Z. Su, J. Chen, G. Badawy, S. Gazibegovic, E. P. A. M. Bakkers, and S. M. Frolov, Triple Andreev dot chains in semiconductor nanowires, [arXiv:2105.08636](https://arxiv.org/abs/2105.08636) [cond-mat.mes-hall].
- [58] T. Dvir, G. Wang, N. van Loo, C.-X. Liu, G. P. Mazur, A. Bordin, S. L. D. ten Haaf, J.-Y. Wang, D. van Driel, F. Zatelli, X. Li, F. K. Malinowski, S. Gazibegovic, G. Badawy, E. P. A. M. Bakkers, M. Wimmer, and L. P. Kouwenhoven, Realization of a minimal Kitaev chain in coupled quantum dots, *Nature (London)* **614**, 445 (2023).
- [59] Ł. Cywiński, R. M. Lutchyn, C. P. Nave, and S. Das Sarma, How to enhance dephasing time in superconducting qubits, *Phys. Rev. B* **77**, 174509 (2008).
- [60] O. E. Dial, M. D. Shulman, S. P. Harvey, H. Bluhm, V. Umansky, and A. Yacoby, Charge noise spectroscopy using coherent exchange oscillations in a singlet-triplet qubit, *Phys. Rev. Lett.* **110**, 146804 (2013).
- [61] J. Yoneda, K. Takeda, T. Otsuka, T. Nakajima, M. R. Delbecq, G. Allison, T. Honda, T. Kodera, S. Oda, Y. Hoshi, N. Usami, K. M. Itoh, and S. Tarucha, A quantum-dot spin qubit with coherence limited by charge noise and fidelity higher than 99.9%, *Nat. Nanotechnol.* **13**, 102 (2018).
- [62] A. Shnirman, Y. Makhlin, and G. Schön, Noise and decoherence in quantum two-level systems, *Phys. Scr.* **T102**, 147 (2002).
- [63] B. M. Freeman, J. S. Schoenfeld, and H. Jiang, Comparison of low frequency charge noise in identically patterned Si/SiO<sub>2</sub> and Si/SiGe quantum dots, *Appl. Phys. Lett.* **108**, 253108 (2016).
- [64] B. Hetényi, P. Boross, and A. Pályi, Hyperfine-assisted decoherence of a phosphorus nuclear-spin qubit in silicon, *Phys. Rev. B* **100**, 115435 (2019).
- [65] J. A. Krzywda and Ł. Cywiński, Adiabatic electron charge transfer between two quantum dots in presence of  $1/f$  noise, *Phys. Rev. B* **101**, 035303 (2020).
- [66] M. Leijnse and K. Flensberg, Introduction to topological superconductivity and Majorana fermions, *Semicond. Sci. Technol.* **27**, 124003 (2012).
- [67] G. Széchenyi and A. Pályi, Parity-to-charge conversion for readout of topological Majorana qubits, *Phys. Rev. B* **101**, 235441 (2020).
- [68] K. Gharavi, D. Hoving, and J. Baugh, Readout of Majorana parity states using a quantum dot, *Phys. Rev. B* **94**, 155417 (2016).
- [69] K. Flensberg, Non-Abelian operations on Majorana fermions via single-charge control, *Phys. Rev. Lett.* **106**, 090503 (2011).
- [70] T. Li, W. A. Coish, M. Hell, K. Flensberg, and M. Leijnse, Four-Majorana qubit with charge readout: Dynamics and decoherence, *Phys. Rev. B* **98**, 205403 (2018).
- [71] J. F. Steiner and F. von Oppen, Readout of Majorana qubits, *Phys. Rev. Res.* **2**, 033255 (2020).
- [72] M. I. K. Munk, J. Schulenburg, R. Egger, and K. Flensberg, Parity-to-charge conversion in Majorana qubit readout, *Phys. Rev. Res.* **2**, 033254 (2020).
- [73] A. Khindanov, D. Pikulin, and T. Karzig, Visibility of noisy quantum dot-based measurements of Majorana qubits, *SciPost Phys.* **10**, 127 (2021).
- [74] P. Boross, J. K. Asbóth, G. Széchenyi, L. Oroszlány, and A. Pályi, Poor man's topological quantum gate based on the Su-Schrieffer-Heeger model, *Phys. Rev. B* **100**, 045414 (2019).
- [75] S. S. Hegde and S. Vishveshwara, Majorana wave-function oscillations, fermion parity switches, and disorder in Kitaev chains, *Phys. Rev. B* **94**, 115166 (2016).
- [76] P. Scarlino, J. H. Ungerer, D. J. van Woerkom, M. Mancini, P. Stano, C. Muller, A. J. Landig, J. V. Koski, C. Reichl, W. Wegscheider, T. Ihn, K. Ensslin, and A. Wallraff, In-situ tuning of the electric dipole strength of a double dot charge qubit: Charge noise protection and ultra strong coupling, *Phys. Rev. X* **12**, 031004 (2022).
- [77] B. Bertrand, H. Flentje, S. Takada, M. Yamamoto, S. Tarucha, A. Ludwig, A. D. Wieck, C. Bäuerle, and T. Meunier, Quantum manipulation of two-electron spin states in isolated double quantum dots, *Phys. Rev. Lett.* **115**, 096801 (2015).
- [78] F. Martins, F. K. Malinowski, P. D. Nissen, E. Barnes, S. Fallahi, G. C. Gardner, M. J. Manfra, C. M. Marcus, and F. Kuemmeth, Noise suppression using symmetric exchange gates in spin qubits, *Phys. Rev. Lett.* **116**, 116801 (2016).
- [79] M. D. Reed, B. M. Maune, R. W. Andrews, M. G. Borselli, K. Eng, M. P. Jura, A. A. Kiselev, T. D. Ladd, S. T. Merkel,

- I. Milosavljevic, E. J. Pritchett, M. T. Rakher, R. S. Ross, A. E. Schmitz, A. Smith, J. A. Wright, M. F. Gyure, and A. T. Hunter, Reduced sensitivity to charge noise in semiconductor spin qubits via symmetric operation, *Phys. Rev. Lett.* **116**, 110402 (2016).
- [80] G. Burkard, T. D. Ladd, A. Pan, J. M. Nichol, and J. R. Petta, Semiconductor spin qubits, *Rev. Mod. Phys.* **95**, 025003 (2023).
- [81] G. Tosi, F. A. Mohiyaddin, V. Schmitt, S. Tenberg, R. Rahman, G. Klimeck, and A. Morello, Silicon quantum processor with robust long-distance qubit couplings, *Nat. Commun.* **8**, 450 (2017).
- [82] J. M. Boter, X. Xue, T. Krähenmann, T. F. Watson, V. N. Premakumar, D. R. Ward, D. E. Savage, M. G. Lagally, M. Friesen, S. N. Coppersmith, M. A. Eriksson, R. Joynt, and L. M. K. Vandersypen, Spatial noise correlations in a Si/SiGe two-qubit device from Bell state coherences, *Phys. Rev. B* **101**, 235133 (2020).
- [83] Y. Makhlin, G. Schon, and A. Shnirman, Dissipation in Josephson qubits, in *New Directions in Mesoscopic Physics (Towards Nanoscience)*, edited by R. Fazio, V. F. Gantmakher, and Y. Imry (Springer, Dordrecht, 2003), pp. 197–224.
- [84] C.-H. Huang, C.-H. Yang, C.-C. Chen, A. S. Dzurak, and H.-S. Goan, High-fidelity and robust two-qubit gates for quantum-dot spin qubits in silicon, *Phys. Rev. A* **99**, 042310 (2019).
- [85] J. R. Petta, A. C. Johnson, J. M. Taylor, E. A. Laird, A. Yacoby, M. D. Lukin, C. M. Marcus, M. P. Hanson, and A. C. Gossard, Coherent manipulation of coupled electron spins in semiconductor quantum dots, *Science* **309**, 2180 (2005).
- [86] C. P. Koch, U. Boscain, T. Calarco, G. Dirr, S. Filipp, S. J. Glaser, R. Kosloff, S. Montangero, T. Schulte-Herbrüggen, D. Sugny, and F. K. Wilhelm, Quantum optimal control in quantum technologies. Strategic report on current status, visions and goals for research in Europe, *EPJ Quantum Technol.* **9**, 19 (2022).